lubricants

MDPI

Article

The Effect of In Situ Boron Reinforcement on the Microstructure and Tribological Performances of a Biocompatible Ti-30Zr-10Ta Alloy Fabricated by Powder Metallurgy

Jorge Chávez [1], Yadira Cruz-Gómez [2], Lorena López-Arámburo [3], Armando M. García-Carrillo [4], Omar Jiménez [3,*], Luis Olmos [5], David Bravo-Barcenas [3] and Martín Flores [3]

[1] Departamento de Ingeniería Mecánica Eléctrica, CUCEI, Universidad de Guadalajara, Blvd. Marcelino García Barragán 1421, Olímpica, Guadalajara 44430, Jalisco, Mexico; jorge.chavez@academicos.udg.mx
[2] Licenciatura en Ciencia de Materiales, Departamento de Física, CUCEI, Universidad de Guadalajara, Blvd. Marcelino García Barragán 1421, Olímpica, Guadalajara 44430, Jalisco, Mexico; yadira.delacruz2021@alumnos.udg.mx
[3] Doctorado en Ciencia de Materiales, Departamento de Ingeniería de Proyectos, CUCEI, Universidad de Guadalajara, José Guadalupe Zuno # 48, Los Belenes, Zapopan 45100, Jalisco, Mexico; lorena.lopez8868@alumnos.udg.mx (L.L.-A.); david.bravo@academicos.udg.mx (D.B.-B.); maflores66@gmail.com (M.F.)
[4] Instituto de Investigación en Metalurgia y Materiales, Universidad Michoacana de San Nicolás de Hidalgo, Ciudad Universitaria, Av. J. Múgica S/N, Col. Felícitas del Río, Morelos, Morelia 58030, Michoacán, Mexico; 2251564a@umich.mx
[5] Instituto de Investigaciones en Ciencias de la Tierra, Universidad Michoacana de San Nicolás de Hidalgo, Ciudad Universitaria, Av. J. Múgica S/N, Col. Felícitas del Río, Morelos, Morelia 58030, Michoacán, Mexico; luis.olmos@umich.mx
* Correspondence: omar.aleman@academicos.udg.mx; Tel.: +52-33-1417-1386

Abstract

This study investigates the impact of in situ boron reinforcement on a biocompatible Ti-30Zr-10Ta alloy produced by powder metallurgy for biomedical applications. This research focused on understanding the influence of boron content (0 to 5 wt.%) on the microstructure, mechanical properties, and tribological behavior of the alloy. The main results showed that increasing boron additions progressively decreased the relative density of the sintered samples. Microstructural analysis via X-ray diffraction (XRD) revealed that the base Ti-30Zr-10Ta alloy exhibited a dominant β-Ti phase with the presence of orthorhombic α'' martensite. The addition of boron led to the in situ precipitation of various borides, specifically TiB, TiB_2, TaB, and TaB_2. Further characterization revealed that the microhardness was enhanced up to 19.6% with lower boron additions, maintaining the elastic modulus of the alloys. Tribological tests demonstrated a significant improvement of 25.7% in wear resistance because of the reinforcement with lower amounts of boride particles. However, higher amounts of boron resulted in a reduction in hardness and elastic modulus at the surface level of 47.2 and 49.3%, respectively, an increase in porosity, and the formation of three-body particles, which contributed to more severe wear and decreased more than twice the wear resistance of the alloy. This research successfully determined the threshold value in a maximum of 0.5 wt.% of boron additions for in situ reinforcement of a biocompatible Ti-30Zr-10Ta alloy suitable for load-bearing applications.

Keywords: titanium composites; biomedical composites; in situ reinforcement; powder metallurgy; tribology

check for updates

Received: 23 August 2025
Revised: 19 September 2025
Accepted: 26 September 2025
Published: 27 September 2025

Citation: Chávez, J.; Cruz-Gómez, Y.; López-Arámburo, L.; García-Carrillo, A.M.; Jiménez, O.; Olmos, L.; Bravo-Barcenas, D.; Flores, M. The Effect of In Situ Boron Reinforcement on the Microstructure and Tribological Performances of a Biocompatible Ti-30Zr-10Ta Alloy Fabricated by Powder Metallurgy. *Lubricants* **2025**, *13*, 431. https://doi.org/10.3390/lubricants13100431

Copyright: © 2025 by the authors. Licensee MDPI, Basel, Switzerland. This article is an open access article distributed under the terms and conditions of the Creative Commons Attribution (CC BY) license (https://creativecommons.org/licenses/by/4.0/).

1. Introduction

Conventional metallic materials, such as cobalt–chromium (Co-Cr) alloys, stainless steel, and titanium (Ti) alloys, have achieved significant success in the biomedical field, fulfilling the increasing global demand for durable and biocompatible materials for implants. Among these, Ti alloys have garnered more attention because of their more balanced properties, including suitable chemical and biomechanical compatibility, compared to other biomedical alloys [1]. However, these alloys still face limitations, such as poor wear resistance, corrosion degradation, and the stress shielding phenomenon, which can lead to implant failure or rejection, requiring revision surgeries and negatively affecting patient outcomes. Additionally, the use of aluminum, vanadium, or nickel as alloying elements can cause neurological diseases, such as Alzheimer's disease, metabolic bone diseases (e.g., osteomalacia), or cytotoxic and allergic responses [2]. While individual alloying elements such as zirconium and tantalum have shown promise in enhancing specific properties, the combined effect of introducing them with in situ reinforcements to develop a material with simultaneously improved biomechanical and tribological characteristics remains a significant, unresolved challenge.

β-Ti alloys have shown great promise in overcoming most biomedical alloy limitations due to their excellent biocompatibility, corrosion resistance, and suitable elastic admissible strain, which is the ratio of σys to E and indicates the biomechanical compatibility of alloys [3]. Different biocompatible elements, such as Ta, Nb, Zr, Mo, and Mn, have been used as β-Ti stabilizers, resulting in alloys with a reduced Young's modulus while maintaining their mechanical strength. Zirconium (Zr), although considered neutral in stabilizing Ti phases, can decrease the phase transition temperature (β-transus) of Ti in the presence of impurities or small amounts of other β-Ti stabilizers [4–6]. Even when used with α-Ti stabilizers, Zr can stabilize the β-Ti phase, as confirmed by M. Musi et al. [7], whose work showed that Zr addition to a Ti-Al alloy lowered the alloy's β-transus temperature. The complete solubility of Zr in the Ti lattice is a key feature that enables controlled solid solution strengthening of the alloys. It has been reported that adding Zr increases the hardness of Ti and reduces its elastic modulus due to changes in the crystal structure [8]. Conversely, K.M Kim et al. [9] studied the effect of Zr addition to a Ti-Nb alloy. They reported that a linear increase in yield strength of up to 57% occurred with 12 at.% Zr. At the same time, the elastic modulus gradually decreased, highlighting the potential of Zr to mitigate the stress-shielding effect and prevent disuse osteopenia [10].

The biomedical use of Ta has been limited due to its high density (16.68 $g \cdot cm^{-3}$) and mechanical strength [11]. However, adding controlled amounts of Ta as an alloying element has been shown to moderately strengthen and increase the malleability of Ti [12]. Additionally, studies on the Ti-Ta binary systems have demonstrated that Ta not only supports the stabilization of the β-Ti phase but also promotes martensitic transformation and reduces the mechanical properties of Ti through alloying elements and processing parameters, which benefits biomedical applications [13–15]. Reports indicate that adding Ta can improve the corrosion performance of Ti alloys in body-simulated solutions due to microstructural changes and the formation of a Ta_2O_5 layer, which offers better protection and stabilization to surfaces than Ti oxides [16,17]. Therefore, Zr and Ta have been shown to enhance the biomechanical compatibility of Ti by aligning its elastoplastic properties more closely with those of human bone.

There have been some investigations into the properties of the Ti-Zr-Ta system. For example, Z. Ruobing et al. [18] have determined the mechanical properties of Ti-Zr-Ta alloys using spark plasma sintering as a consolidation technique. The results showed that the addition of Zr and Ta increased microhardness and yield strength while effectively decreasing the elastic modulus of the tested materials due to stabilization of the β-Ti phase.

This resulted in values ranging between 35 and 50 GPa, which is close to the elastic modulus of human bone (5–30 GPa). On the other hand, the balance between alloying elements is crucial for achieving better alloy performance. In this context, results presented in an investigation by A. Biesiekierski et al. [19] showed that higher yield strength and plasticity were attained with the composition Ti-30Zr-22Ta, which has the lower Zr content and the highest Ta addition, resulting in the lower elastic modulus measured for all tested alloys and improving the biomechanical properties of Ti alloys.

Despite the biocompatibility and biomechanical resistance of Ti alloys, their well-known poor tribological properties are attributed to their low performance against plastic shearing, limited work hardening ability, and insufficient protection from surface oxides [20]. Certainly, adding elements that reduce the mechanical properties of Ti, such as the elastic modulus, can decrease its tribological resistance. However, in situ particle reinforcement for creating composite materials benefits from the limited solubility between certain elements, leading to the precipitation of hard intermetallic phases that improve mechanical properties and reduce wear [21]. This approach has a clear advantage over ex- situ methods by fostering strong interfacial bonding between the matrix and the reinforcement phase. Several studies have confirmed the formation of carbides and borides during the synthesis of β-Ti alloys by incorporating ceramic powders, such as NbC, NbB_2, B_4C [22], TiB_2 [23], and BN [24], or special materials such as carbon nanotubes [25]. Among these, boron-rich particles are particularly favored in forming Ti matrix composites because boron is a lightweight element that can act as a strong strengthener in metallic alloys, influencing grain refinement [26]. Additionally, boron additions to Ti can enable in- situ synthesis of borides, which demonstrate high compatibility and strong interfacial bonding with Ti. Coupled with their high hardness, these borides contribute to improved tribological and tribocorrosive performance [27]. However, the amount of boron added must be carefully controlled to achieve the optimal balance of mechanical properties and wear resistance. It has been reported that the wear resistance of a Ti6Al4V matrix produced by powder bed fusion improves progressively with boron additions up to 1.5 wt.% [28]. This improvement is attributed to grain refinement, which causes a linear increase in hardness with boron addition and the formation of TiB particles. Furthermore, Qi An et al. [23] created network-structured TiBw/Ti6Al4V composites via powder metallurgy, noting that although mechanical properties increased with reinforcement additions (up to 12 vol.%), wear loss tended to rise due to reduced abrasive resistance, driven by decreased plasticity and the detachment of TiB_2 particles.

This study examines for the first time the effects of different boron additions to a Ti-30Zr-10Ta alloy designed for potential biomedical applications, aiming to determine the threshold of boron use needed to improve the tribological performance of materials. The base composition was chosen because Zr and Ta can enhance mechanical properties, and Ti is known for its biocompatibility and corrosion resistance. The alloys were made using a conventional powder metallurgy (PM) technique, which is cost-effective and versatile, suitable for creating complex shapes and controlling microstructure. Additionally, adding boron as an alloying element is believed to modify the microstructure and, as a result, improve the mechanical properties and wear behavior of the Ti-30Zr-10Ta base alloy, which has been thoroughly studied to identify the most suitable compositions.

2. Materials and Methods

2.1. Sample Preparation

This study utilized high-purity metal particles of Ti, Zr, Ta, and B (purity of 99.95%) as raw materials (Figure 1). The Ti-30Zr-10Ta-xB (x = 0, 0.1, 0.3, 0.5, 1, 3 and 5 wt.%) system of alloys was prepared using the conventional powder metallurgy route. The powders for

each composition were mixed using a Turbula for 30 min in a vacuum-sealed container to prevent oxidation. For each sample, 1 wt.% of polyvinyl alcohol was used as a binder for powders. Green compacts of 10 mm diameter and 5 mm height were obtained by cold compaction using a universal testing machine and a stainless-steel die, with a pressure of 400 MPa applied at 0.5 mm·s^{-1}. Then, the relative density was calculated from the measured density of compacts, which was obtained by considering the weight and the volume of each compact, and the theoretical density (ρt) estimated with the rule of mixtures: ρt = ρ1f1 + ρ2f2 + . . . + ρnfn, where ρ1, ρ2 and ρn are the densities and f1, f2 and fn are the fractions of the constituent metals, respectively.

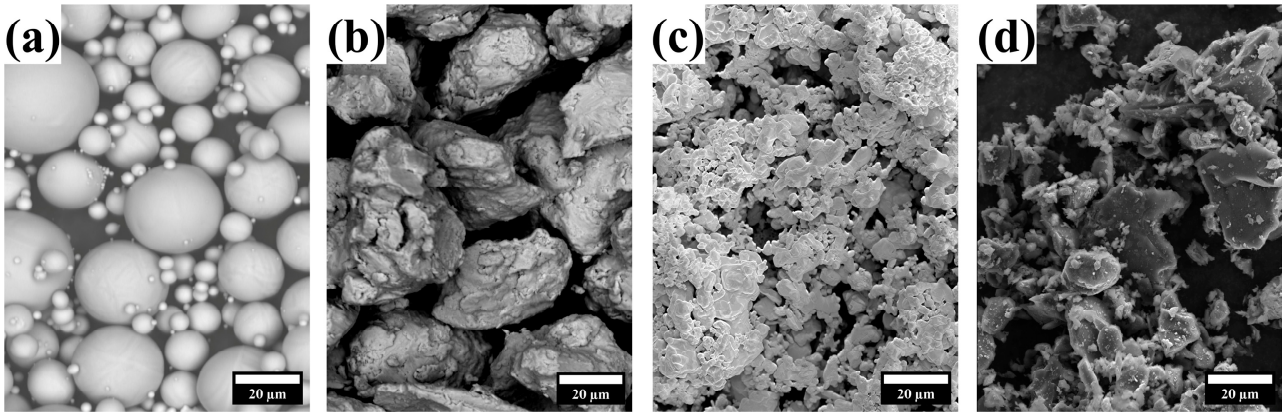

Figure 1. SEM micrographs of the raw powders used for the Ti-30Zr-10Ta-*x*B fabrication: (**a**) Ti, (**b**) Zr, (**c**) Ta and (**d**) B particles.

For the consolidation of green compacts, solid-state sintering was performed in a vacuum atmosphere (4 × 10^2 Pa) using a horizontal tube furnace. The thermal cycle for sintering was designed as follows: a first stage at 500 °C for 45 min, intended for binder elimination, and a second stage at the sintering temperature of 1300 °C for 60 min. Both stages were reached with a heating rate of 10 °C·min^{-1} and were cooled within the furnace to room temperature. The employed sintering parameters were selected as function of previous results, which exploratorily demonstrated to generate high dense Ti alloys. After sintering, the relative density of the samples was estimated using the above-described procedure to evaluate the final porosity in the alloys.

2.2. Microstructural and Hardness Characterization

For the microstructural characterization of Ti-30Zr-10Ta-*x*B alloys, the samples were cross-sectioned and then metallographic preparation of the sections was performed by mounting, grinding with SiC sandpapers of varying grain sizes (80 to 2500), and polishing with 1 and 0.05 µm alumina solutions to obtain a mirror-like surface. The microstructure of the alloys was evaluated on images obtained from the polished cross-sections by means of scanning electron microscopy (SEM) acquired with a JEOL JSM-7600F field emission scanning electron microscope (Akishima, Tokyo, Japan) equipped with energy dispersive X-ray spectroscopy (EDS) from Bruker xFlash Detector 6 | 30 and the phase constitutions were determined by X-ray diffraction (XRD) using an Empyrean Panalytical diffractometer. Microhardness was determined by Vickers microindentation tests performed on the polished surface of the alloys using a Future Tech FM-800 microhardness tester (Future-Tech Corp., Kanawana, Japan), with a load of 300 gf and a dwell time of 15 s for each indentation. At least 15 indentations were made on each sample to ensure the statistical validity of the results. The microhardness tests were performed following the ASTM E384-22 standard [29]. Additionally, to obtain low-scale hardness and elastic modulus, instrumented

indentation tests were conducted using a Nanovea CB500 mechanical tester (Irvine, CA, USA). 10 indentations with a diamond Berkovich three-sided pyramid tip (calibrated before measurement on fused silica to maintain accuracy) were performed. The maximum load used was 50 mN, with a loading/unloading rate of $mN \cdot s^{-1}$. Elastoplastic parameters, such as the hardness and reduced elastic modulus, were calculated from the load–displacement curves using the procedure proposed by Oliver and Pharr [30].

2.3. Tribological Tests

Dry reciprocating sliding tests were conducted to evaluate the wear behavior of the Ti-30Zr-10Ta-*x*B alloys. A CETR-UMT2 (Campbell, CA, USA) microtribometer in a linear ball-on-flat reciprocating configuration was employed, which constantly recorded the CoF values resulting from wear tests. All tests were performed on the polished cross-sections of samples applying a constant load of 1 N at the reciprocating frequency of 1 Hz, using a stroke length of 5 mm for 1800 s. A non-conductive 3 mm alumina ball (~780 HV) was selected as a counterpart. The selected tribological pair developed a maximum Hertzian contact pressure of ~570 MPa, which exceeded the highest human hip joints of 12 MPa [31] but allowed to test the tribological performance of materials. The tests were at ambient temperature (25 °C) and controlled humidity of 40%. Each test was repeated three times to ensure the repeatability of results. After testing, the volume of the wear tracks was measured using a Filmetrics® Profilm3D® Optical Profilometer (Milpitas, CA, USA) and the specific wear rate of the tests was calculated from the measured values. The morphological characterization of the wear tracks was conducted through the analysis of SEM images to establish the wear mechanisms that occurred during the tests.

3. Results and Discussion

3.1. Densification of Samples

The relative density of samples in both green and sintered states is shown in Figure 2. As observed, the relative density of green compacts is not affected by the amount of B, reaching values close to that of the 0B sample. This suggests proper particle assembly during the rearrangement of particles with different mechanical properties, shapes, and sizes in the green compacts. Additionally, the sintering process caused densification of the samples due to coalescence between particles with higher solubility, such as Ti-Zr and Ti-Ta pairs [32,33], which enhances powder sinterability and allows the base alloy to achieve relatively high density values. However, Zr-Ta pairs are an exception; according to the equilibria diagram [34], their very limited solubility at low temperatures increases only above the eutectoid temperature (~1060 °C) and is restricted by a miscibility gap, which limits the sintering of this pair and reduces their contribution to the final densification. Although a reasonable densification of 22% was achieved, this effect prevented the 0B sample from reaching a relative density comparable to other Ti-Zr alloys made by powder metallurgy (98%) [35]. Furthermore, the addition of boron gradually decreased the relative density of the base alloy. This decline is linked to the solid insolubility between boron and the components of the base alloy, as well established in the binary phase diagrams [36–38]. Consequently, unreacted boron particles and intermetallic formations can hinder particle contact, impede solid-state sintering, and promote pore formation, ultimately reducing the densification of the samples.

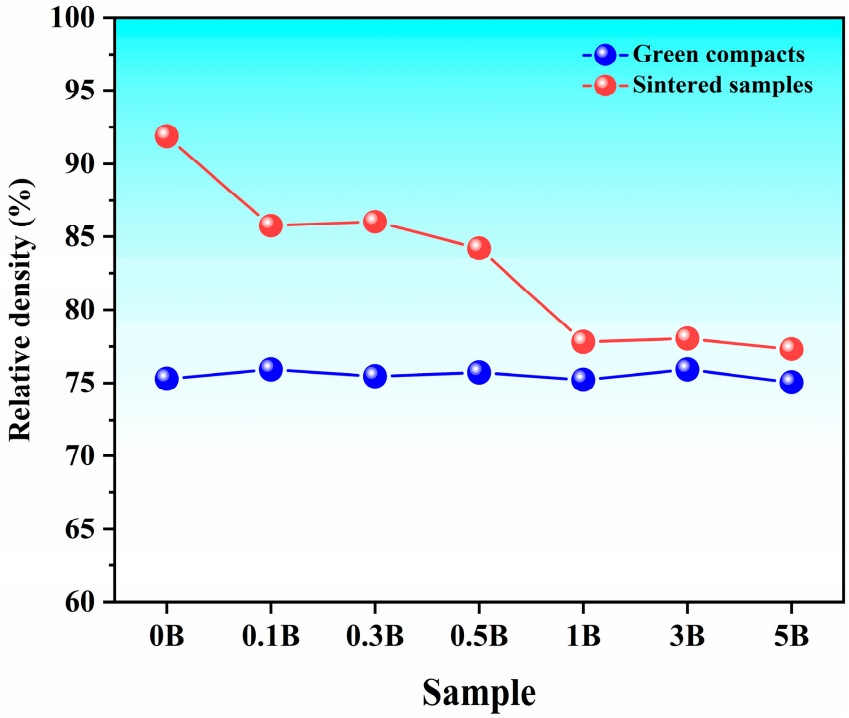

Figure 2. Effect of boron additions on the relative density of the Ti-30Zr-10Ta green compacts and sintered samples.

3.2. Microstructural Analysis

Figure 3 shows the diffraction patterns of the sintering samples. As observed, the pattern of the 0B sample mainly consists of reflections corresponding to the bcc β-Ti, which was identified using PDF 44-1288 from the ICSD database. Additionally, Ta reflections (04-0788) are present in the base alloy, indicating the existence of undissolved particles. Although Zr is considered a neutral element for phase stabilization of Ti, it has been found that Zr can exert a β-Ti stabilization effect depending on the content of other β-stabilizing elements and impurities [4]. Therefore, the amount of Ta, a strong β-stabilizer, produced a significant stabilizing effect on the β-Ti phase in the 0B sample [39]. Furthermore, the pattern of the 0B sample also shows a martensitic orthorhombic α'' phase with a space group Cmcm, which is an intermediate structure formed during the $\beta \rightarrow \alpha'$ transformation, especially with higher concentrations of β-stabilizing elements [40]. A.V. Dobromyslov et al. [41,42] investigated the formation of the orthorhombic α'' phase in various binary Ti and Zr alloys by quenching from the β phase and using different alloying elements. They reported α'' formation with elements such as Ta, Mo, Nb, W, Re, and Ru, with the maximum occurrence in the Ti-Ta system. However, Zr was excluded as a causative factor in the transformation due to the size mismatch, meaning the α'' phase does not form when this mismatch exceeds a certain level.

The heat treatment parameters heavily influence the formation of martensitic phases, as shown by S. Guo et al. [43] for Ti-Nb alloys. They report that a solution treatment at 800 °C followed by quenching has a greater potential to induce the α'' transformation than using lower treatment temperatures. Conversely, earlier studies demonstrated the martensitic transformation of Ti64-xTa alloys made by powder metallurgy, emphasizing how alloying element dissolution affects martensitic phase formation, even at slower cooling rates than those used in quenching.

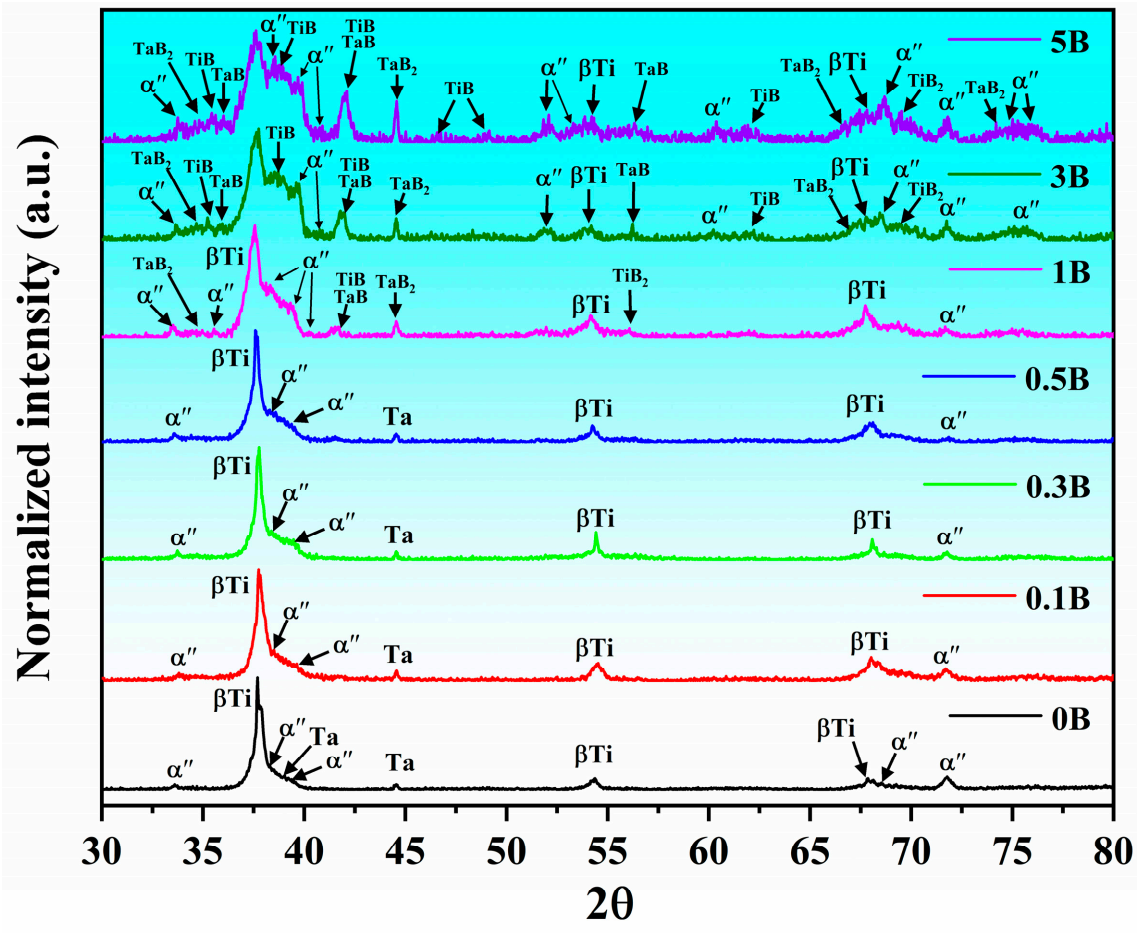

Figure 3. X-ray diffraction patterns for phase determination of Ti-30Zr-10Ta sintered samples with different boron additions.

The addition of small amounts (0.1–0.5 wt.%) of boron does not seem to affect the structure of the Ti-30Zr-10Ta alloys. However, adding 1 to 5 wt.% results in the appearance of new reflections that correspond to the in situ precipitation of various boron intermetallics combined with the other alloy elements. The formation of intermetallic phases can be predicted by analyzing the change in Gibbs free energy (ΔG_{mix}) for the formation of these compounds [44]. In Table 1, the calculated ΔH_{mix} and ΔG_{mix} values for the potential pairs in the alloys are shown [45]. Based on the ΔG values for the possible pairs involving boron, considering a 1:1 ratio at the contact point during sintering, the formation likelihood sequence appears to be Zr-B → Ti-B → Ta-B. Because the 2θ range between 37.5 and 40° is crowded with peaks that appear with boron addition, the ΔG sequence helps identify phases in the XRD patterns shown in Figure 3. As a result, intermetallic phases such as TiB_2 (35-0741), TiB (05-0700), TaB_2 (38-1462), and TaB (35-0815) were identified in the samples with higher boron content. Although distinguishing between TiB_2 and TaB_2 is challenging because they share the same structure and have similar reflections, the peaks near 69.7° in 2θ allowed us to identify the formation and growth of a TiB_2 phase in the samples with the highest boron additions. Moreover, even though Zr-B interactions are more likely, reflections of zirconium borides were not detected in the XRD patterns of the alloys. This can be attributed to Zr depletion caused by diffusion between Ti and Zr during sintering [32], leading to solid solutions (with positive enthalpies listed in Table 1) that promoted boron formation with undissolved Ta particles, thus exceeding the Ti content in the matrix.

Table 1. Thermodynamic parameters for possible pairs interactions in the Ti-30Zr-10Ta-xB alloys.

Pairs	ΔH_{mix} (kJ·mol^{-1})	ΔG_{mix} (kJ·mol^{-1})
Zr-Ta	3	−2.7628
Ti-Ta	1	−4.7628
Ti-Zr	0	−5.7628
Ta-B	−54	−59.763
Ti-B	−58	−63.763
Zr-B	−71	−76.763

Furthermore, increasing the boron content resulted in a corresponding rise in the α'' phase, as shown by the increased intensity of the reflections. Several factors can contribute to the growth of α'' martensite in a Ti alloy. For instance, boron additions can potentially decrease the martensitic temperature, affecting the kinetics of martensite formation [46]. Additionally, lattice strain caused by the solid solution of foreign elements into the Ti lattice can enhance the martensitic transformation, as explored by W. Mei et al. [47] for a Ti-V alloy and by H. Fang et al. [48] for a Ti-22Nb alloy with Al and Ta additions. Moreover, the interfaces between intermetallic precipitates and the matrix alloy can act as heterogeneous nucleation sites, promoting the martensitic transformation, as studied at the atomic level for Ti in the work of Q.J. Chen et al. [49].

Metallographies of the Ti-30Zr-10Ta alloys with boron additions are shown in Figure 4. As seen, the grain boundaries of equiaxed β-Ti grains are visible within the base alloy matrix. A very low level of chemical etching was used to observe the microstructure without affecting the visualization of in situ reinforcing particles. Remaining closed pores due to incomplete coalescence of particles, a characteristic of the conventional sintering process, are observed in samples with low boron concentrations (Figure 4a–d). The porosity of these samples increased slightly with boron addition. However, in samples with higher boron levels (Figure 4e–g), porosity increased significantly, resulting in open, interconnected pores caused by the obstruction effect of boron particles on contact between matrix particles. A contribution to this high porosity level is also from the in situ reaction of boron particles forming intermetallic phases detected in the XRD analysis. Based on the ΔG values of reactions between the alloy components and boron, high exothermic responses are expected during the formation of these intermetallics, which can increase porosity in the matrix [50]. The porosity observed in the samples aligns well with the relative density shown in Figure 2.

As shown in Figure 4, for the samples with lower boron additions, only a few intermetallic clusters precipitate on the matrix alloy, and their number increases with more boron added. Clearly, the limited number of intermetallic clusters and their locations do not hinder contact between the matrix particles, suggesting that the decrease in relative density observed in the 0B sample is mainly due to reactions during intermetallic formation. However, for samples with higher boron additions, intermetallic clusters form near the matrix particles, leading to porosity. Micrographs of the 0B and 5B samples acquired using BSE are shown in Figure 5. In Figure 5a, the prior β-Ti equiaxed grains are outlined by grain boundaries, which display a fine needle-like microstructure corresponding to the α'' transformation of the base alloy that occurred during sintering [51].

The image shown in Figure 5b was captured at the same magnification as the one for the 0B sample (Figure 5a); therefore, a clear coarsening of the martensite needles is observed. The primary morphological difference between the hcp α' and orthorhombic α'' martensitic phases of Ti is the needle size, with α'' exhibiting a coarser structure than α' due to the supersaturated solid solution of elements in the α-Ti phase [52]. Therefore, the coarsening of the martensite needles is directly related to the increase in the amount of the α'' phase.

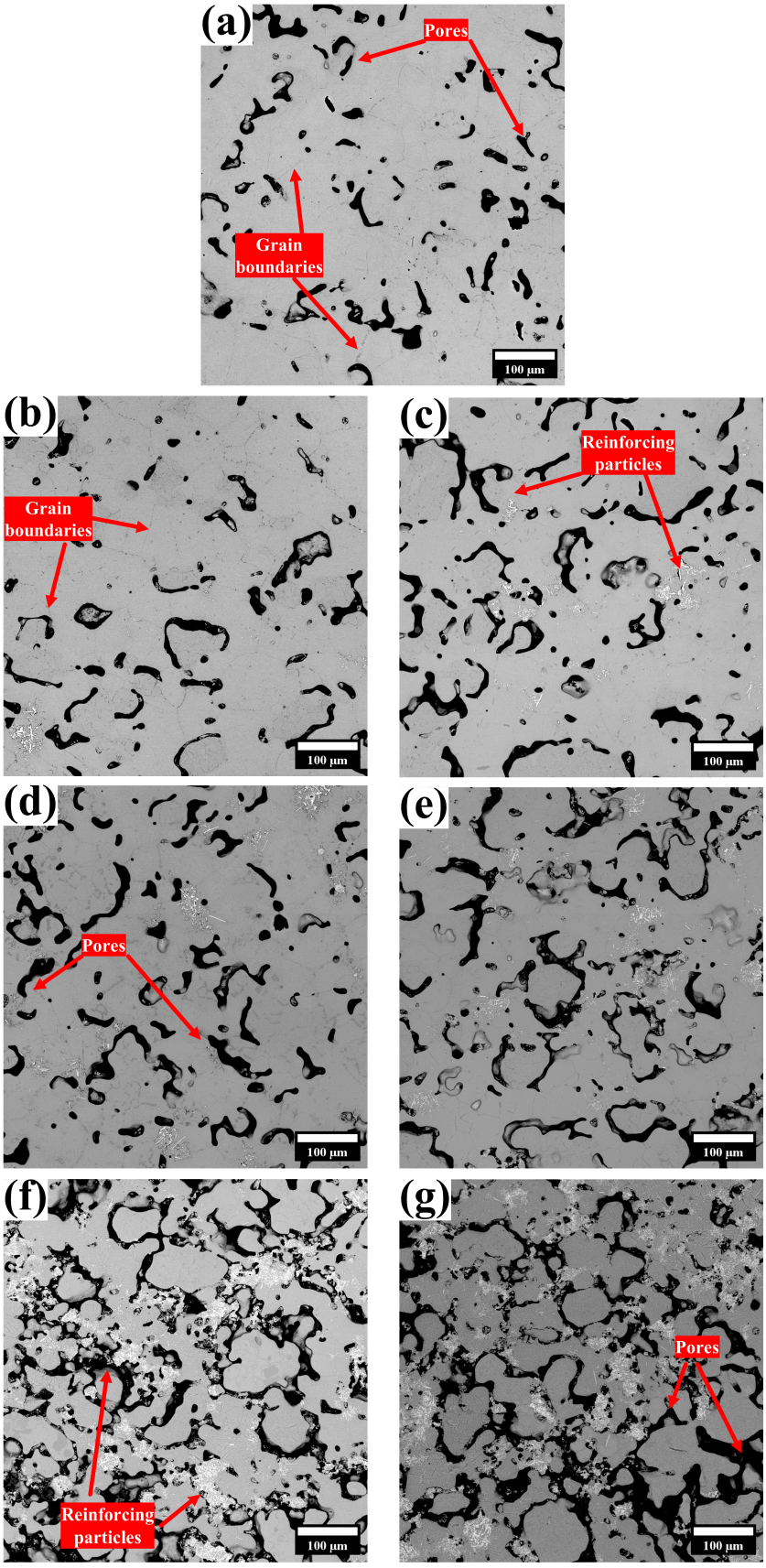

Figure 4. Backscatter electron microscopy (BSE) images of the cross-sections of the Ti-30Zr-10Ta sintered samples with (**a**) 0, (**b**) 0.1, (**c**) 0.3, (**d**) 0.5, (**e**) 1, (**f**) 3 and (**g**) 5 wt.% of boron.

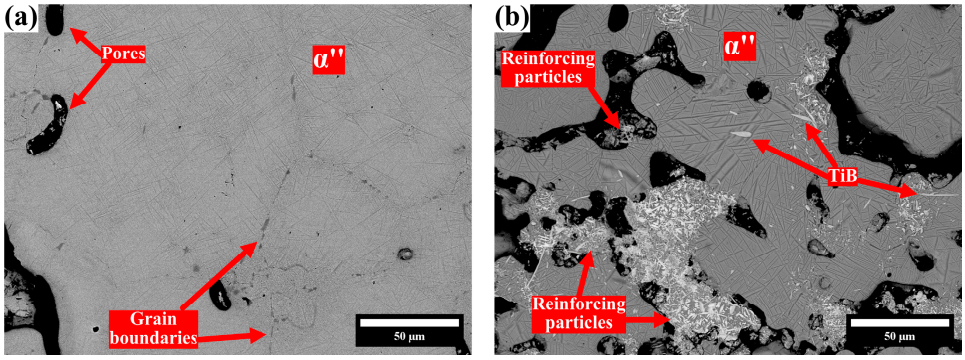

Figure 5. Backscatter electron microscopy (BSE) images of the (**a**) 0B and (**b**) 5B sintered samples.

Additionally, Figure 5b, which shows the other samples containing boron, reveals a slight contrast between the intermetallic particles and the matrix. This contrast is caused by differences in atomic numbers, which are distinguished by the BSE technique. The image illustrates the location and distribution of the intermetallic particles, which were synthesized in situ within the matrix alloy and inside the pores. In this image, TiB whiskers are visible within the matrix. The TiB whiskers resulted from a coherent reaction between Ti and boron particles, Ti + B → TiB, possibly formed from TiB_2 particles that were depleted to create TiB, according to the reaction Ti + TiB_2 → 2TiB. Both reactions occur spontaneously due to their lower free energy (see Table 1) [28,53]. In Figure 6, EDS mappings of the 5B alloy are shown, illustrating the distribution of elements within the microstructure. The main elements in the alloy—Ti, Zr, and Ta—are distributed throughout the analyzed area, with Zr- and Ta-rich zones resulting from incomplete particle diffusion. Although identifying light elements like boron using EDS is challenging, EDS mapping enables the detection of boron concentrations dispersed throughout the matrix and located mainly in quiet zones, as particles within the Ta-rich regions. As observed in the reference SEM image, boron particle accumulations are primarily composed of Ta and boron. These are clearly identified by their whisker shape, which is characteristic of Ti and Ta borides.

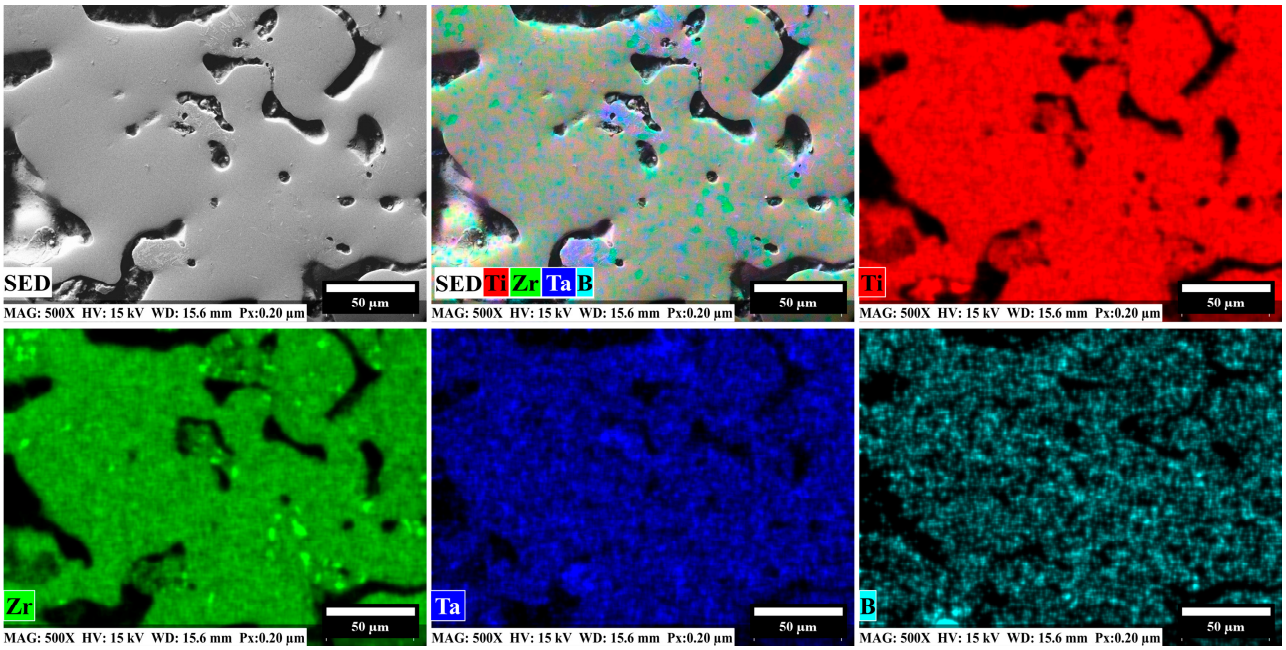

Figure 6. SEM images and EDS elemental mappings of Ti, Zr, Ta, and B of the microstructures of the Ti-30Zr-10Ta-5B alloy.

3.3. Microhardness Evaluation

Hardness is a key mechanical property that strongly correlates with a material's wear resistance, as it indicates the material's ability to resist plastic deformation and surface damage [54]. In this context, the hardening resulting from the solid solution of elements into a Ti matrix and the precipitation of reinforcing phases plays a vital role in the alloy's wear behavior. The Vickers microhardness values for the samples in this study are shown in Figure 7. As observed, the microhardness of the 0B sample exceeds that of Ti-Zr alloys produced through powder metallurgy, which had a maximum of 343 HV [35]. This difference is attributed to the high level of solid solution hardening achieved during processing, which is due to the 10 wt.% of Ta in the base alloy, as explored by the authors elsewhere [55]. Conversely, the lowest boron additions increased the microhardness of the Ti-30Zr-10Ta alloy by up to 19.6%, reaching the maximum at 0.3 wt.% boron. This increase can be attributed to the dissolution of boron into the base alloy lattice, resulting in effective hardening. Additionally, higher boron concentrations led to increased porosity levels, resulting in a reduction in microhardness, which leveled off at around 500 HV in the samples with the highest boron content. Unlike the microhardness improvements observed in a Ti6Al4V alloy reinforced with similar boron percentages [28], the results presented here demonstrate the effectiveness of the reinforcement despite notable decreases in relative density.

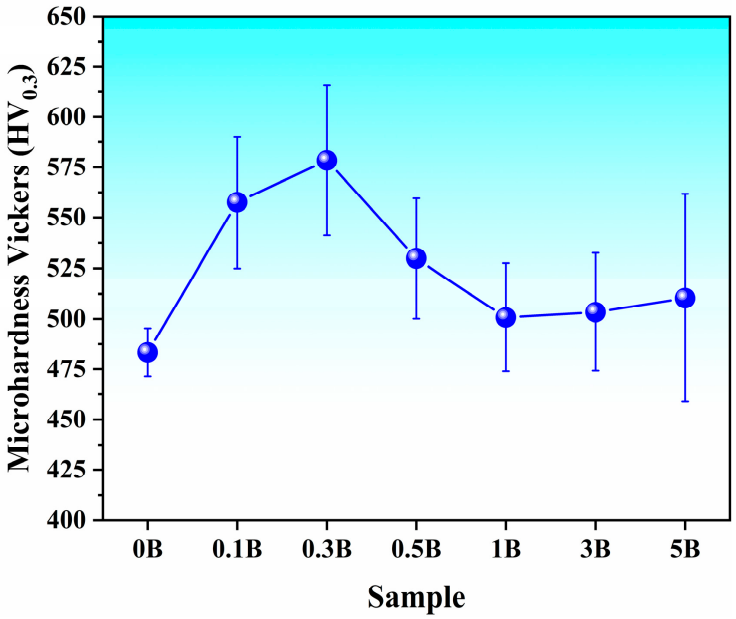

Figure 7. Vickers microhardness of the Ti-30Zr-10Ta sintered samples as a function of the boron addition.

3.4. Tribological Behavior

The representative coefficient of friction (CoF) versus time for the samples in their polished condition is shown in Figure 8a. A rapid increase in CoF at the start of the test indicated the formation of dynamic contact between the counterpart and the sample surfaces. Afterwards, the CoF of the 0B sample stabilized at 0.52 and remained steady throughout the test. Samples with lower boron content behaved similarly to the sample without boron, maintaining relatively constant CoF values around 0.52, which suggests that small boron additions did not influence the contact behavior compared to the 0B sample. In contrast, samples with the highest boron content showed a gradual increase in CoF over time during testing, leveling off after 1200 s of sliding and reaching CoF values of 0.58, 0.64,

and 0.68 for the 1B, 3B, and 5B samples, respectively. This steady rise in CoF indicates more severe wear caused by three-body wear from loose intermetallic particles.

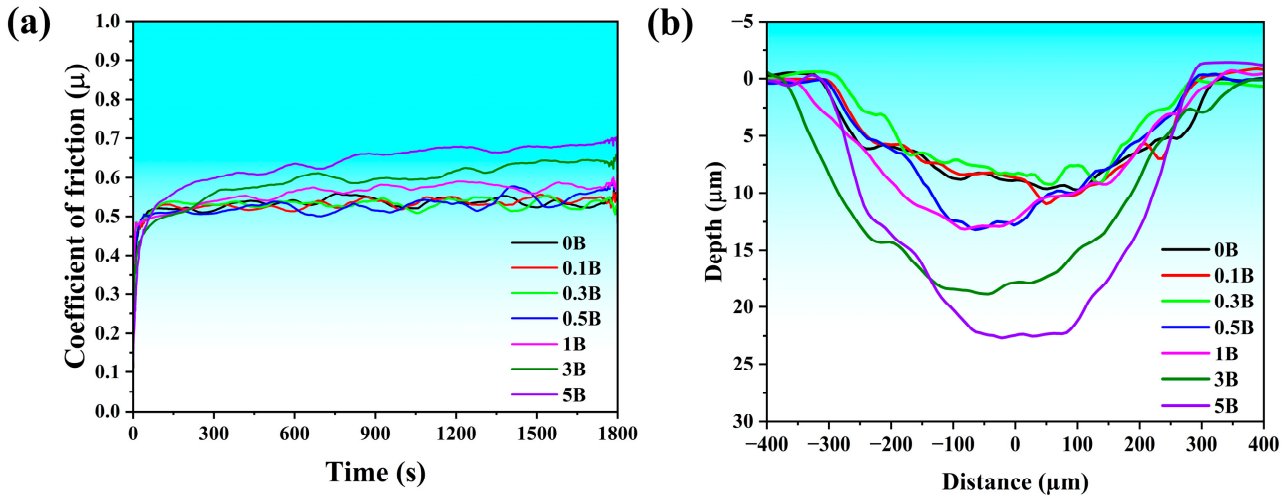

Figure 8. (**a**) Coefficient of friction recorded during the reciprocating test and (**b**) wear profiles obtained from the center of the wear tracks of Ti-30Zr-10Ta samples with different boron additions.

In Figure 8b, representative profiles obtained perpendicularly to the center (half of the stroke) of the wear tracks are shown. The wear profiles of the 0B and 0.1B samples are quite similar, indicating that the lowest boron addition had no effect on the depth or width of the Ti-30Zr-10Ta alloy. In contrast, the profile of the 0.3B sample is the narrowest and has the lowest depth of all samples. Additionally, although the 0.5B and 1B samples reached the same depth, the 0.5B sample is narrower, indicating less wear. Finally, the profile of the 3B sample is the widest, while the profile of the 5B sample is the deepest. Clearly, the depth of the wear tracks corresponds to the microhardness trend shown in Figure 7 and the CoF values discussed earlier (Figure 8a). The differences in profile width are due to variations in wear severity along the tracks, caused by loose intermetallic particles acting as a three-body abrasive.

Figure 9 shows the specific wear rates calculated from volume loss measured using optical profilometry. The analysis indicated that adding 0.1 wt.% boron had no significant effect on the wear rate of the Ti-30Zr-10Ta alloy. However, the 0.3B sample exhibited the lowest wear rate (3.9×10^{-4} $mm^3 \cdot N^{-1} \cdot m^{-1}$), demonstrating the highest wear resistance among all samples. This reduction in wear rate represents a 25.5% decrease compared to the unreinforced sample. The primary reason for this decrease is likely the hardening caused by boron's dissolution into the base alloy lattice. Nonetheless, the 0.3B sample showed the highest microhardness value, resulting from a balanced combination of solid solution hardening, relative density, and minimal intermetallic formation, as previously discussed. These factors contributed to the mechanical properties that provided the alloy with greater wear resistance. The wear rate values for these samples were lower than those reported for commercially pure Ti produced by powder metallurgy (5.65×10^{-4} $mm^3 \cdot N^{-1} \cdot m^{-1}$) [56]. This highlights the importance of solution hardening in the Ti-30Zr-10Ta alloy reinforced with small amounts of boron. The effect of solution hardening on the wear resistance of Ti alloys has been studied by B. Vinod Et Al. [57], who found that increased microhardness resulting from the addition of elements led to a decrease in wear loss.

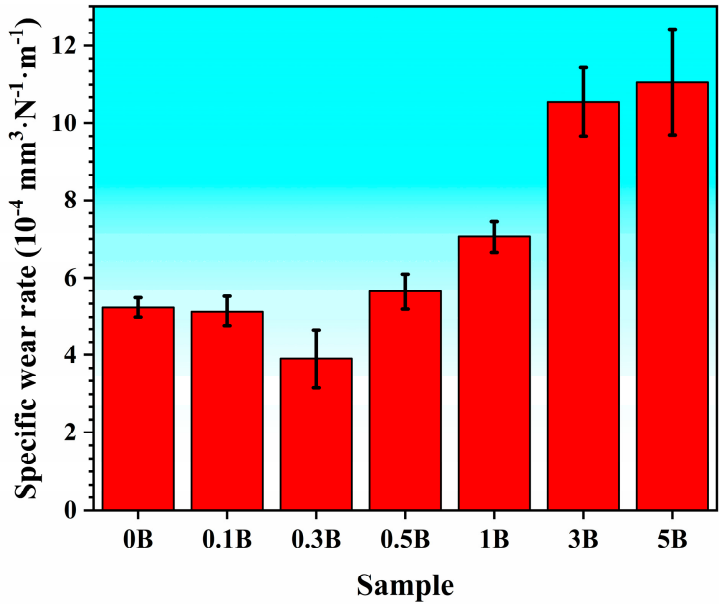

Figure 9. Specific wear rates calculated from the volumes of the wear tracks of Ti-30Zr-10Ta samples with different boron additions.

The specific wear rate of Ti-30Zr-10Ta increases gradually with additional boron, becoming significant for the 3B and 5B samples. As shown by the CoF values, boron addition affects severe wear, indicating that the in situ formed borides act as three-body particles, which alter the wear mechanism and lead to more material being removed from the tracks. It has been noted that adding 2 wt.% boron to a TNZT alloy causes an increase in wear rates due to the loss of TiB particles, resulting in a higher CoF [58]. More recent studies have shown that adding 0.5 wt.% boron improves the wear resistance of a similar alloy (TNZT) [59]. Both studies used the laser-engineered net shaping process, which involves melting the materials. Comparing these results helps determine the safe limits for adding boron to a Ti alloy produced by melting. In this study, the maximum safe boron addition is established at 0.3 wt.%, as processing characteristics like porosity in powder metallurgy set a lower limit, though it still offers benefits for the alloy.

Although the wear rates of the samples follow the microhardness trend, determining the wear mechanism is essential to elucidate the contribution of the overall characteristics of the alloys and the role of the reinforcement particles, which can act as three-body abrasives that increase the wear, to the wear rates achieved by the samples. In order to evaluate the wear mechanisms involved in the dry wear of the Ti-30Zr-10Ta alloy with boron additions, SEM images of the worn surface acquired at the center of the wear tracks are shown in Figure 10. As observed, abrasion is the primary wear mechanism present in all samples, characterized by the formation of grooves aligned with the sliding direction. Those grooves were created by the material that was pulled out of the matrix (debris) and were dragged until they adhered to the surface. Plastic deformation zones were also detected, which are the sources for the dragged material. The plastic deformation in the sliding surface of a metallic material is often associated with a low strain hardening ability, which is accompanied by low resistance to shear stress [28]. Additionally, the plasticity of the surfaces is indicated by the dragged material filling the pores, as shown in Figure 10a, allowing for the determination of plastic deformation as the secondary mechanism dominating the wear of Ti-30Zr-10Ta alloys with low boron concentrations.

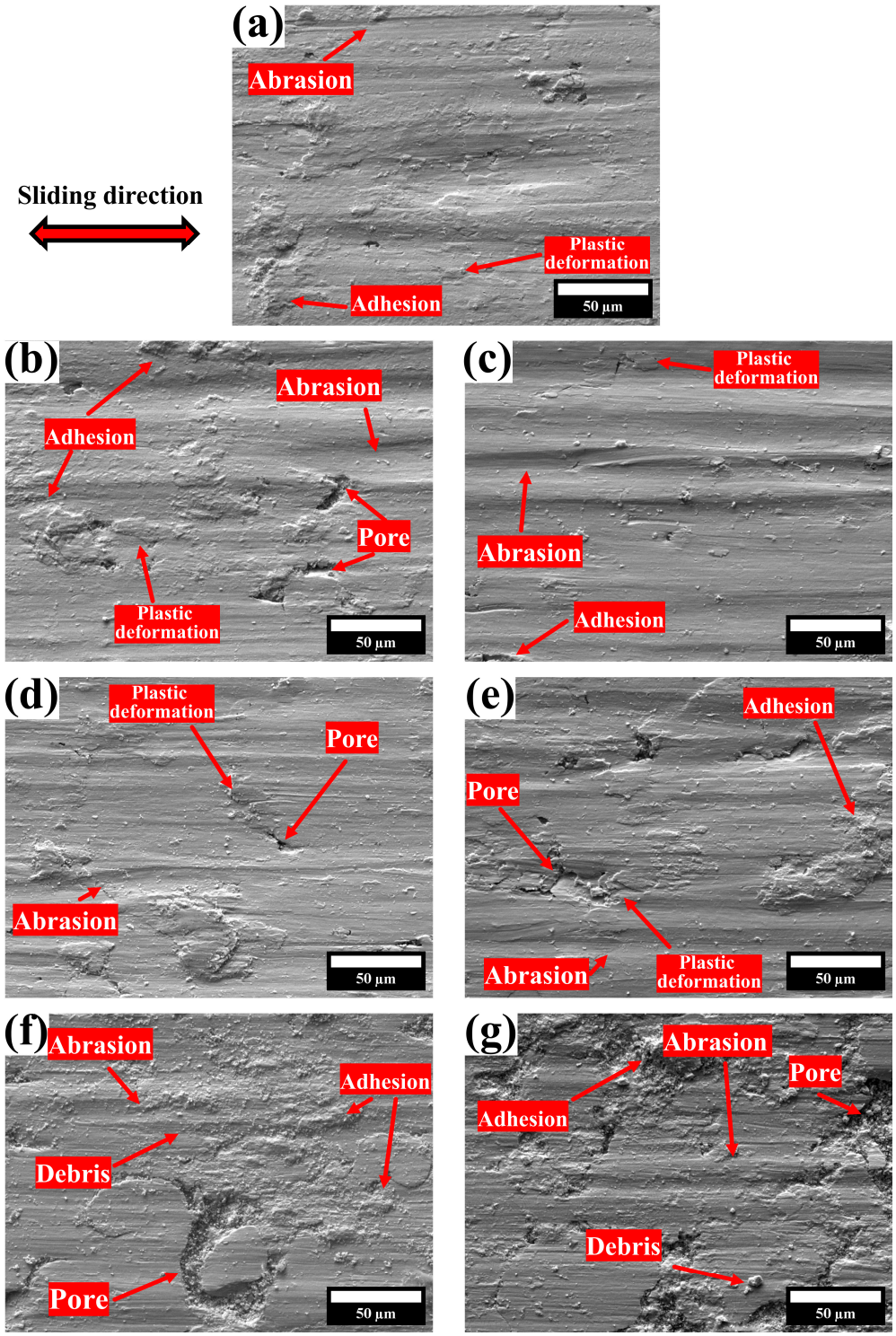

Figure 10. Secondary electron SEM micrographs of worn surface of the Ti-30Zr-10Ta sintered samples with (**a**) 0, (**b**) 0.1, (**c**) 0.3, (**d**) 0.5, (**e**) 1, (**f**) 3 and (**g**) 5 wt.% of boron.

On the other hand, as shown in the images of Figure 10f,g, larger adhesions and clusters of particles or debris can be seen attached to the surfaces of the wear tracks, along with plastic-deformed zones in the sliding direction. As observed in the higher magnification images of Figure 11, more pronounced and deeper abrasion grooves are noticeable in the sample with 5% wt. of boron compared to the Ti-30Zr-10Ta-based alloy, indicating that the greater number of intermetallic particles caused more severe wear in the alloys.

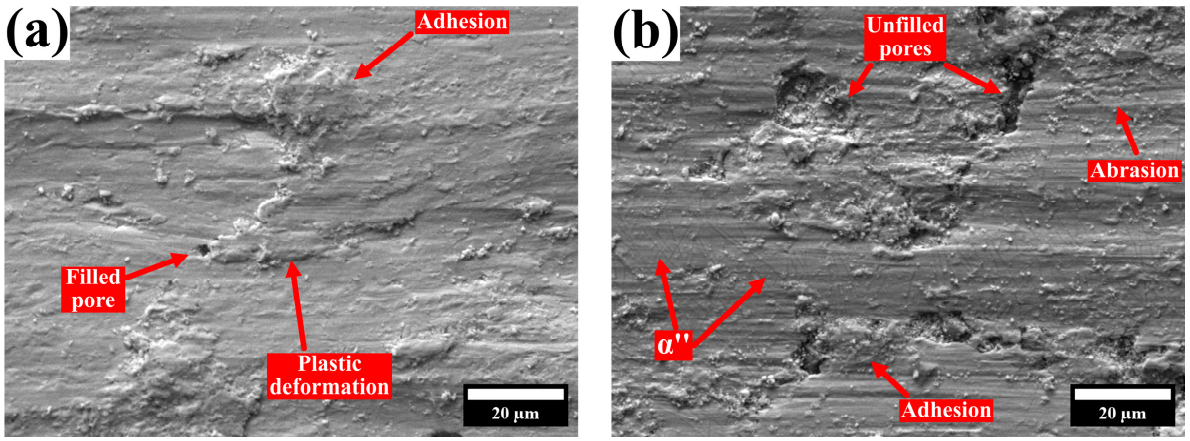

Figure 11. High magnification of secondary electron SEM micrographs of worn surface of the Ti-30Zr-10Ta sintered samples with (**a**) 0, (**b**) 5 wt.% of boron.

In order to elucidate the surface elastoplastic values of composite materials, Figure 12a depicts the results of the instrumented indentation performed with a 50 mN load and a Berkovich indenter on the polished surfaces of samples. As observed, a decreasing trend in both hardness and elastic modulus was obtained as a function of boron addition. It has been reported that a martensitic transformation to an orthorhombic α'' phase results in the softening of Ti alloys, decreasing the mechanical properties such as elastic modulus and yield strength but increasing the plastic strain ability of Ti-Zr alloys [60,61]. Additionally, the analysis of the elemental mapping presented in Figure 13, which corresponds to the wear track surface performed on the sample with the addition of 5 wt.% of boron, allowed the detection that material adhered to the surface is mainly composed of Ta and boron, indicating that hard tantalum borides clusters were attached to the surface track. Thus, in this work, it is believed that the Ta consumption that occurs during intermetallic formation with boron is capable of reducing the solid solution hardening of the matrix, contributing to a decrease in the mechanical properties and, therefore, to the wear increment of alloys. Consequently, the wear resulted in more severe damage due to the excess loss of intermetallic particles, acting as three-body particles that abrade a softer matrix with higher levels of porosity. These factors contributed to the higher levels of wear, as shown in Figure 9.

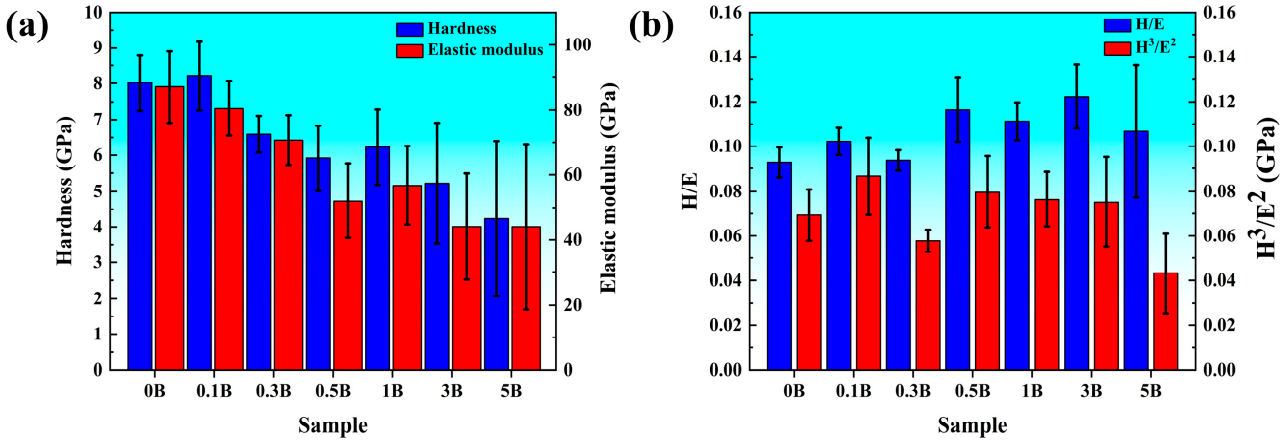

Figure 12. (**a**) Hardness and elastic modulus obtained by instrumented indentation and (**b**) the H/E and H^3/E^2 ratios of polished surfaces of Ti-30Zr-10Ta samples with different boron additions.

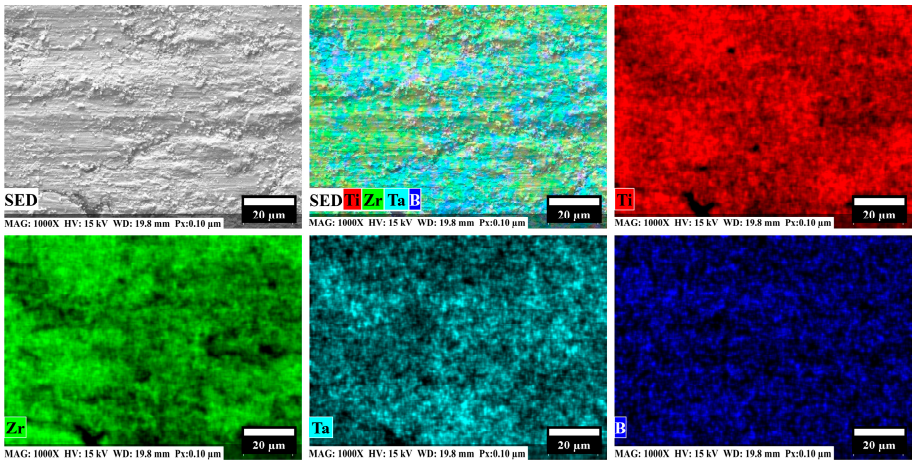

Figure 13. SEM images and EDS elemental mappings of worn surface of the Ti-30Zr-10Ta-5B sin-tered sample.

The hardness and elastic modulus values obtained from the samples in this study are comparable to those reported for other biomedical Ti-based alloys, such as the Ti-Fe-xTa alloys examined by S. Ehtemam-Haghighi et al. [62], who achieved maximum hardness values of approximately 5.7 GPa, decreasing with Ta addition to 3.38 GPa. Additionally, the elastic modulus of Ti-30Zr-10Ta was similar to the around 80 GPa reported for the martensitic Ti–13Zr–13Nb studied by P. Majumdar et al. [63]. The reduction in elastic modulus with boron addition brought values closer to 24.5 GPa, the maximum elastic modulus reported for human bone [64], highlighting the biomechanical potential of the alloys tested here. Furthermore, the results from the instrumented indentation technique are valuable for determining parameters that help understand surface responses to load applications, thus enabling the elucidation and correlation of mechanisms during sliding wear [65]. The H/E ratio is used to assess a material's resistance to elastic strain and its relation to wear resistance [66]. Meanwhile, H^3/E^2 indicates the material's resistance to plastic deformation under load [67]. As shown in Figure 12b, the H/E values of Ti-30Zr-10Ta tend to increase due to the rise in the martensitic α'' phase of Ti caused by boron addition, which results in a softer material than β-Ti, as previously mentioned. Conversely, the H^3/E^2 parameter tends to increase with the lowest boron addition (0.1B), then slightly decrease with higher additions (0.5B to 5B). An anomaly was observed with 0.3B, which decreased in value, diverging from the trend. According to Figures 7 and 9, respectively, this sample showed the highest microhardness and the lowest wear rate among all samples; therefore, it can be inferred that the uneven diffusion of elements in this sample created zones with high elastic modulus values, reducing the calculated H^3/E^2.

4. Conclusions

In this work, a Ti-30Zr-10Ta alloy with varying boron additions was successfully fabricated by using the conventional powder metallurgy route. A study was conducted to investigate the effect of boron additions on the microstructure and mechanical properties, aiming to establish the tribological performance of the in situ composites and determine the relevance of their proposal as a potential biomedical material. The following conclusion could be drawn based on the obtained results:

- XRD and SEM analysis demonstrated that the Ti-30Zr-10Ta alloy mainly comprised β-Ti and the α'' phases. Additionally, the boron additions resulted in both the increase in the martensitic α'' phase amount and the in situ precipitation of intermetallic phases such as TiB, TaB, and TaB_2, mainly configured as whiskers.

- Boride formation progressively reduced the relative density of the sintered samples due to the hindrance of sinterable contacts. Despite the density decrease, the solid solution of boron in the matrix caused the alloy to harden by up to 19.63% with lower boron additions (0.3 wt.%); however, this trend diminished with further additions due to increased porosity and the consumption of Ta to form borides.
- Instrumented indentation confirmed a consistent decrease in both hardness and elastic modulus as the boron content increased, which was attributed to the increase in a softer martensitic α'' phase with higher boron levels. Furthermore, the H/E ratio indicated a more elastic contact with the increase in martensite, and the H^3/E^2 parameter showed higher wear resistance in samples with lower boron addition, which declined with greater reinforcement.
- The Ti-30Zr-10Ta alloy with 0.3 wt.% boron exhibited the highest wear resistance, demonstrating a 25.5% reduction in wear rate compared to the unreinforced alloy. For samples with higher boron content (1, 3, and 5 wt.%), the wear rate and coefficient of friction increased, as the in situ formed boride particles acted as a three-body abrasive, causing more severe wear.

The findings indicate that an optimal boron addition of 0.3 wt.% is necessary for this specific alloy system to achieve the best combination of mechanical properties and wear resistance for potential biomedical applications. This emphasizes the importance of carefully controlling the boron content to maximize benefits while reducing the adverse effects of porosity and excessive intermetallic formation. Mechanical alloying is expected to enhance the dissolution of elements, prevent segregation, and mitigate reductions in mechanical properties and higher levels of porosity, which can lead to increased wear damage observed at higher boron concentrations.

Author Contributions: J.C.: conceptualization, methodology, formal analysis and writing—original draft preparation; Y.C.-G.: conceptualization, methodology, investigation, formal analysis; L.L.-A.: investigation, conceptualization, methodology, formal analysis; A.M.G.-C.: methodology, investigation; O.J.: funding acquisition, resources and project administration; L.O.: investigation; D.B.-B.: investigation; M.F.: investigation. All authors have read and agreed to the published version of the manuscript.

Funding: This research received no external funding.

Data Availability Statement: The raw/processed data required to reproduce these findings cannot be shared at this time as the data also form part of an ongoing study.

Acknowledgments: This research was supported by the Secretary for Science, Humanities, Technology and Innovation (SECIHTI) via Doctoral Scholarship of L. López (CVU 867008). The authors would also like to thank all the institutions and staff involved in this investigation.

Conflicts of Interest: The authors declare that they have no conflicts of interest.

References

1. Baskaran, P.; Muthiah, B.; Uthirapathy, V. A systematic review on biomaterials and their recent progress in biomedical applications: Bone tissue engineering. *Rev. Inorg. Chem.* **2025**. [CrossRef]
2. Nouri, A.; Hodgson, P.; Wen, C. *Biomimetic Porous Titanium Scaffolds for Orthopedic and Dental Applications*; Mukherjee, A., Ed.; Biomimetics Learning from Nature, Chapter 21; InTech: Rijek, Croatia, 2010.
3. Li, S.; Kang, S.W.; Kim, J.H.; Nam, T.-H.; Yeom, J.-T. Superelastic metastable Ti-Mo-Sn alloys with high elastic admissible strain for potential bio-implant applications. *J. Mater. Sci. Technol.* **2023**, *163*, 45–58. [CrossRef]
4. Abdel-Hady, M.; Fuwa, H.; Hinoshita, K.; Kimura, H.; Shinzato, Y.; Morinaga, M. Phase stability change with Zr content in β-type Ti–Nb alloys. *Scr. Mater.* **2007**, *57*, 1000–1003. [CrossRef]
5. Si, K.; Wang, X.; Yin, Z.; Yang, Y.; Wu, S.; Li, G.; Zhang, K.; Wang, H.; Huang, A. Influence of Oxygen and Zirconium Contents on the Mechanical Properties of Ti-23Nb-0.7Ta-Zr-O Alloys. *Metals* **2022**, *12*, 1018. [CrossRef]

6. Gonzalez, E.D.; Fukumasu, N.K.; Afonso, C.R.M.; Nascente, P.A.P. Impact of Zr content on the nanostructure, mechanical, and tribological behaviors of β-Ti-Nb-Zr ternary alloy coatings. *Thin Solid Film.* **2021**, *721*, 138565. [CrossRef]
7. Musi, M.; Kardos, S.; Hatzenbichler, L.; Holec, D.; Stark, A.; Allen, M.; Güther, V.; Clemens, H.; Spoerk-Erdely, P. The effect of zirconium on the Ti-(42-46 at.%)Al system. *Acta Mater.* **2022**, *241*, 118414. [CrossRef]
8. Sharma, A.; Waddell, J.N.; Li, K.C.; Sharma, L.A.; Prior, D.J.; Duncan, W.J. Is titanium–zirconium alloy a better alternative to pure titanium for oral implant? Composition, mechanical properties, and microstructure analysis. *Saudi Dent. J.* **2021**, *33*, 546–553. [CrossRef]
9. Kim, K.M.; Kim, H.Y.; Miyazaki, S. Effect of Zr Content on Phase Stability, Deformation Behavior, and Young's Modulus in Ti–Nb–Zr Alloys. *Materials* **2020**, *13*, 476. [CrossRef]
10. Franzone, J.M.; Sargent, B.M.; Do, A.N.D.; Knue, M.; Marini, J.C.; Kruse, R.W. Stress Shielding in the Setting of Osteogenesis Imperfecta and the Effect of Downsizing an Intramedullary Rod: A Case Report. *JBJS Case Connect.* **2021**, *11*, e20. [CrossRef]
11. Li, H.; Yao, Z.; Zhang, J.; Cai, X.; Li, L.; Liu, G.; Liu, J.; Cui, L.; Huang, J. The progress on physicochemical properties and biocompatibility of tantalum-based metal bone implants. *SN Appl. Sci.* **2020**, *2*, 671. [CrossRef]
12. Wang, C.; Cai, Q.; Liu, J.; Yan, X. Strengthening mechanism of lamellar-structured Ti–Ta alloys prepared by powder metallurgy. *J. Mater. Res. Technol.* **2022**, *21*, 2868–2879. [CrossRef]
13. Lauhoff, C.; Nobach, M.; Medvedev, A.; Arold, T.; Torrent, C.; Elambasseril, J.; Krooß, P.; Stenzel, M.; Weinmann, M.; Xu, W.; et al. Electron beam powder bed fusion of Ti-30Ta high-temperature shape memory alloy: Microstructure and phase transformation behaviour. *Virtual Phys. Prototyp.* **2024**, *19*, e2358107. [CrossRef]
14. Chávez, J.; Alemán, O.J.; Martínez, M.F.; Vergara-Hernández, H.J.; Olmos, L.; Garnica-González, P.; Bouvard, D. Characterization of Ti6Al4V–Ti6Al4V/30Ta Bilayer Components Processed by Powder Metallurgy for Biomedical Applications. *Met. Mater. Int.* **2020**, *26*, 205–220. [CrossRef]
15. Kuroda, P.A.B.; dos Santos, R.F.M.; Grandini, C.R.; Afonso, C.R.M. Unveiling the effect of Nb and Zr additions on microstructure and properties of β Ti-25Ta alloys for biomedical applications. *Mater. Charact.* **2024**, *207*, 113577. [CrossRef]
16. Dercz, G.; Matuła, I.; Zubko, M.; Kazek-Kęsik, A.; Maszybrocka, J.; Simka, W.; Dercz, J.; Świec, P.; Jendrzejewska, I. Synthesis of porous Ti–50Ta alloy by powder metallurgy. *Mater. Charact.* **2018**, *142*, 124–136. [CrossRef]
17. Zhao, D.; Han, C.; Li, Y.; Li, J.; Zhou, K.; Wei, Q.; Liu, J.; Shi, Y. Improvement on mechanical properties and corrosion resistance of titanium-tantalum alloys in-situ fabricated via selective laser melting. *J. Alloys Compd.* **2019**, *804*, 288–298. [CrossRef]
18. Zhang, R.; Lin, A. First principles study of Ti-Zr-Ta alloy phase stability and elastic properties. *Mater. Res. Express* **2023**, *10*, 026503.
19. Biesiekierski, A.; Ping, D.; Li, Y.; Lin, J.; Munir, K.S.; Yamabe-Mitarai, Y.; Wen, C. Extraordinary high strength Ti-Zr-Ta alloys through nanoscaled, dual-cubic spinodal reinforcement. *Acta Biomater.* **2017**, *53*, 549–558. [CrossRef]
20. Hussein, M.A.; Mohammed, A.S.; Al-Aqeeli, N. Wear Characteristics of Metallic Biomaterials: A Review. *Materials* **2015**, *8*, 2749–2768. [CrossRef]
21. Pooja, K.; Tarannum, N.; Chaudhary, P. Metal matrix composites: Revolutionary materials for shaping the future. *Discov. Mater.* **2025**, *5*, 35. [CrossRef]
22. Gonçalves, V.R.M.; Corrêa, D.R.N.; Sousa, T.d.S.P.d.; Pintão, C.A.F.; Grandini, C.R.; Afonso, C.R.M.; Lisboa-Filho, P.N. Promising composites for wear resistant load-bearing implant applications: Low elastic moduli of β Ti–Nb alloy reinforced with TiC particles and/or TiB whiskers. *J. Mater. Res. Technol.* **2024**, *30*, 879–889. [CrossRef]
23. An, Q.; Huang, L.; Bao, Y.; Zhang, R.; Jiang, S.; Geng, L.; Xiao, M. Dry sliding wear characteristics of in-situ TiBw/Ti6Al4V composites with different network parameters. *Tribol. Int.* **2018**, *121*, 252–259. [CrossRef]
24. Otte, J.A.; Zou, J.; Patel, R.; Lu, M.; Dargusch, M.S. TiB Nanowhisker Reinforced Titanium Matrix Composite with Improved Hardness for Biomedical Applications. *Nanomaterials* **2020**, *10*, 2480. [CrossRef] [PubMed]
25. Li, S.; Sun, B.; Imai, H.; Kondoh, K. Powder metallurgy Ti–TiC metal matrix composites prepared by in situ reactive processing of Ti-VGCFs system. *Carbon* **2013**, *61*, 216–228. [CrossRef]
26. Chen, K.; Zhu, C.; He, J.; Zhang, X.-Y.; Zhou, K. Unexpected strengthening and toughening effects of B minor alloying in a new low-density near-α titanium alloy. *Scr. Mater.* **2025**, *254*, 116318. [CrossRef]
27. Sousa, L.; Alves, A.; Costa, N.; Gemini-Piperni, S.; Rossi, A.; Ribeiro, A.; Simões, S.; Toptan, F. Preliminary tribo-electrochemical and biological responses of the Ti-TiB-TiCx in-situ composites intended for load-bearing biomedical implants. *J. Alloys Compd.* **2022**, *896*, 162965. [CrossRef]
28. Verma, P.K.; Warghane, S.; Nichul, U.; Kumar, P.; Dhole, A.; Hiwarkar, V. Effect of boron addition on microstructure, hardness and wear performance of Ti-6Al-4 V alloy manufactured by laser powder bed fusion additive manufacturing. *Mater. Charact.* **2021**, *172*, 110848. [CrossRef]
29. *ASTM 384-22*; Standard Test Method for Microindentation Hardness of Materials. ASTM Committee: West Conshohocken, PA, USA, 2022.
30. Oliver, W.C.; Pharr, G.M. An improved technique for determining hardness and elastic modulus using load and displacement sensing indentation experiments. *J. Mater. Res.* **1992**, *7*, 1564–1583. [CrossRef]

31. Dantas, P.; Grenho, A.; Mascarenhas, V.; Martins, J.; da Silva, M.T.; Gonçalves, S.B.; Consciência, J.G. Hip joint contact pressure and force: A scoping review of in vivo and cadaver studies. *Bone Jt. Res.* **2023**, *12*, 712–721. [CrossRef]
32. Murray, J.L. The Ti-Zr (Titanium-Zirconium) system. *Bull. Alloy Phase Diagr.* **1981**, *2*, 197–201. [CrossRef]
33. Murray, J.L. The Ta-Ti (Tantalum-Titanium) system. *Bull. Alloy Phase Diagr.* **1981**, *2*, 62–66. [CrossRef]
34. Fernández Guillermet, A. Phase diagram and thermochemical properties of the Zr–Ta system. An assessment based on Gibbs energy modelling. *J. Alloys Compd.* **1995**, *226*, 174–184. [CrossRef]
35. Amigó-Mata, A.; Haro-Rodriguez, M.; Vicente-Escuder, Á.; Amigó-Borrás, V. Development of Ti–Zr alloys by powder metallurgy for biomedical applications. *Powder Metall.* **2022**, *65*, 31–38. [CrossRef]
36. Murray, J.L.; Liao, P.K.; Spear, K.E. The B−Ti (Boron-Titanium) system. *Bull. Alloy Phase Diagr.* **1986**, *7*, 550–555. [CrossRef]
37. Franke, P.; Neuschütz, D.; Scientific Group Thermodata Europe (SGTE). Introduction: Thermodynamic Properties of Inorganic Materials. In *Binary Systems. Part 5: Binary Systems Supplement 1: Phase Diagrams, Phase Transition Data, Integral and Partial Quantities of Alloys*; Springer: Berlin/Heidelberg, Germany, 2007; pp. 1–13.
38. Sobolev, A.S.; Kuz'MA, Y.B.; Soboleva, T.E.; Fedorov, T.F. Phase equilibria in tantalum—Titanium—Boron and tantalum—Molybdenum—Boron systems. *Sov. Powder Metall. Met. Ceram.* **1968**, *7*, 48–51. [CrossRef]
39. Hulka, I.; Mirza-Rosca, J.C.; Buzdugan, D.; Saceleanu, A. Microstructure and Mechanical Characteristics of Ti-Ta Alloys before and after NaOH Treatment and Their Behavior in Simulated Body Fluid. *Materials* **2023**, *16*, 1943. [CrossRef] [PubMed]
40. Lütjering, G.; Williams, J.C. *Titanium*; Springer: Berlin/Heidelberg, Germany, 2007.
41. Dobromyslov, A.V. Nature and Regularities of the Orthorhombic α″-Phase Formation in Binary Titanium Alloys. *Alloys* **2023**, *2*, 148–156. [CrossRef]
42. Dobromyslov, A.V.; Taluts, N.I. Regularities of Orthorhombic α″ Phase Formation in Binary Zirconium Alloys. *Metall. Mater. Trans. A* **2025**, *56*, 3961–3971. [CrossRef]
43. Guo, S.; Zhang, J.; Cheng, X.; Zhao, X. A metastable β-type Ti–Nb binary alloy with low modulus and high strength. *J. Alloys Compd.* **2015**, *644*, 411–415. [CrossRef]
44. Saunders, N.; Miodownik, A.P. (Eds.) Chapter 3—Basic Thermodynamics. In *Pergamon Materials Series*; Pergamon Press: Oxford, UK, 1998; pp. 33–57.
45. Takeuchi, A.; Inoue, A. Classification of Bulk Metallic Glasses by Atomic Size Difference, Heat of Mixing and Period of Constituent Elements and Its Application to Characterization of the Main Alloying Element. *Mater. Trans.* **2005**, *46*, 2817–2829. [CrossRef]
46. Horiuchi, Y.; Inamura, T.; Kim, H.Y.; Wakashima, K.; Miyazaki, S.; Hosoda, H. Effect of Boron Concentration on Martensitic Transformation Temperatures, Stress for Inducing Martensite and Slip Stress of Ti-24 mol%Nb-3 mol%Al Superelastic Alloy. *Mater. Trans.* **2007**, *48*, 407–413. [CrossRef]
47. Mei, W.; Sun, J.; Wen, Y. Martensitic transformation from β to α′ and α″ phases in Ti–V alloys: A first-principles study. *J. Mater. Res.* **2017**, *32*, 3183–3190. [CrossRef]
48. Fang, H.; Xu, X.; Zhang, H.; Sun, Q.; Sun, J. Alloying Effect on Transformation Strain and Martensitic Transformation Temperature of Ti-Based Alloys from Ab Initio Calculations. *Materials* **2023**, *16*, 6069. [CrossRef] [PubMed]
49. Chen, Q.-J.; Ma, S.-Y.; Wang, S.-Q. The Nucleation and the Intrinsic Microstructure Evolution of Martensite from 332 ⟨113⟩ β Twin Boundary in β Titanium: First-Principles Calculations. *Metals* **2019**, *9*, 1202. [CrossRef]
50. Kayani, S.H.; Cui, M.; Ahmed, R.T.M.; Cho, Y.-H.; Lee, J.-M.; Park, N.-K.; Ajmal, H.M.S.; Euh, K. Pore formation mechanism and intermetallic phase transformation in Ti–Al alloy during reactive sintering. *J. Mater. Res. Technol.* **2023**, *22*, 1878–1887. [CrossRef]
51. Hu, X.; Liu, C.; Wu, Z.; Song, M. Formation mechanism of β precipitate within α′ martensite in α+β titanium alloys. *Scr. Mater.* **2025**, *262*, 116632. [CrossRef]
52. Motyka, M. Martensite Formation and Decomposition during Traditional and AM Processing of Two-Phase Titanium Alloys—An Overview. *Metals* **2021**, *11*, 481. [CrossRef]
53. Angel, D.A.; Mikó, T.; Kristály, F.; Benke, M.; Gácsi, Z. Development of TiB and nanocrystalline Ti-reinforced novel hybrid Ti nanocomposite produced by powder metallurgy. *J. Mater. Sci.* **2022**, *57*, 4130–4144. [CrossRef]
54. Rundora, N.R.; Klenam, D.E.P.; Polat, S.; Mathabathe, N.M.; van der Merwe, J.; Bodunrin, M.O. Dry Sliding Wear Behavior of Experimental Low-Cost Titanium Alloys. *Tribol. Trans.* **2024**, *67*, 560–572. [CrossRef]
55. Chávez, J.; Jimenez, O.; Olmos, L.; Farias, I.; Flores-Jimenez, M.; Suárez-Martínez, R.; Cabezas-Villa, J.; Lemus-Ruiz, J. Tribocorrosion behavior of Ti64-xTa alloys fabricated through powder metallurgy. *Mater. Lett.* **2020**, *280*, 128590. [CrossRef]
56. Avcu, Y.Y.; Iakovakis, E.; Guney, M.; Çalım, E.; Özkılınç, A.; Abakay, E.; Sönmez, F.; Koç, F.G.; Yamanoğlu, R.; Cengiz, A.; et al. Surface and Tribological Properties of Powder Metallurgical Cp-Ti Titanium Alloy Modified by Shot Peening. *Coatings* **2023**, *13*, 89. [CrossRef]
57. Vinod, B.; Suresh, S.; Reddy, S.S.K. Tribological and Fatigue Behaviour of Ti-Nb-Zr-Sn Alloy through Powder Compacting: Novel Performance of High Niobium Alloys for Bone Tissue Compatibility. *Arch. Metall. Mater.* **2024**, *69*, 1543–1554. [CrossRef]
58. Samuel, S.; Nag, S.; Scharf, T.W.; Banerjee, R. Wear resistance of laser-deposited boride reinforced Ti-Nb–Zr–Ta alloy composites for orthopedic implants. *Mater. Sci. Eng. C* **2008**, *28*, 414–420. [CrossRef]

59. Mantri, S.A.; Torgerson, T.; Ivanov, E.; Scharf, T.W.; Banerjee, R. Effect of boron addition on the mechanical wear resistance of additively manufactured biomedical titanium alloy. *Metall. Mater. Trans. A* **2018**, *49*, 806–810. [CrossRef]
60. Jiang, X.; Jing, R.; Ma, M.; Liu, R. The orthorhombic α'' martensite transformation during water quenching and its influence on mechanical properties of Ti-41Zr-7.3Al alloy. *Intermetallics* **2014**, *52*, 32–35. [CrossRef]
61. Ji, P.; Chen, B.; Li, B.; Tang, Y.; Zhang, G.; Zhang, X.; Ma, M.; Liu, R. Influence of Nb addition on microstructural evolution and compression mechanical properties of Ti-Zr alloys. *J. Mater. Sci. Technol.* **2021**, *69*, 7–14. [CrossRef]
62. Ehtemam-Haghighi, S.; Cao, G.; Zhang, L.-C. Nanoindentation study of mechanical properties of Ti based alloys with Fe and Ta additions. *J. Alloys Compd.* **2017**, *692*, 892–897. [CrossRef]
63. Majumdar, P.; Singh, S.; Chakraborty, M. The role of heat treatment on microstructure and mechanical properties of Ti–13Zr–13Nb alloy for biomedical load bearing applications. *J. Mech. Behav. Biomed. Mater.* **2011**, *4*, 1132–1144. [CrossRef]
64. Zysset, P.K.; Guo, X.E.; Hoffler, C.E.; E Moore, K.; A Goldstein, S. Elastic modulus and hardness of cortical and trabecular bone lamellae measured by nanoindentation in the human femur. *J. Biomech.* **1999**, *32*, 1005–1012. [CrossRef]
65. Beake, B.D. The influence of the H/E ratio on wear resistance of coating systems—Insights from small-scale testing. *Surf. Coat. Technol.* **2022**, *442*, 128272. [CrossRef]
66. Finkin, E. Examination of abrasion resistance criteria for some ductile metals. *J. Lubr. Technol.* **1974**, *96*, 210–214. [CrossRef]
67. Tsui, T.Y.; Pharr, G.M.; Oliver, W.C.; Bhatia, C.S.; White, R.L.; Anders, S.; Anders, A.; Brown, I.G. Nanoindentation and Nanoscratching of Hard Carbon Coatings for Magnetic Disks. *MRS Online Proc. Libr.* **1995**, *383*, 447–452. [CrossRef]

Disclaimer/Publisher's Note: The statements, opinions and data contained in all publications are solely those of the individual author(s) and contributor(s) and not of MDPI and/or the editor(s). MDPI and/or the editor(s) disclaim responsibility for any injury to people or property resulting from any ideas, methods, instructions or products referred to in the content.